

Adsorption of water on the pristine and defective semiconducting 2D CrPX₃ monolayers (X: S, Se)

Sifan Xu¹, Zhicheng Wu¹, Yuriy Dedkov^{1,2,*}, and
Elena Voloshina^{1,2,*}

¹Department of Physics, Shanghai University, 99 Shangda Road, 200444 Shanghai, China

²Institut für Chemie und Biochemie, Freie Universität Berlin, Arnimallee 22, 14195 Berlin, Germany

Abstract.

The effect of vacancy and water adsorption on the electronic structure of semiconducting 2D trichalcogenide material CrPX₃ (X: S, Se) is studied using state-of-the-art density functional theory (DFT) approach. It is found that chalcogen vacancies play a minor role on the electronic structure of CrPX₃ in the vicinity of the Fermi level leading to the slightly reduced band gap for these materials, however, inducing strongly localised defect states which are placed in the energy gap formed by the valence band states. Our DFT calculations show that the interaction of water molecules with CrPX₃, pristine and defective, can be described as physisorption and the adsorption energy for H₂O is insensitive to the difference between pristine and chalcogen-defective surface of trichalcogenide material. These results are the first steps for the theoretical description of the ambient molecules interaction with 2D semiconducting CrPX₃ material, that is important for its future experimental studies and possible applications.

1. Introduction

The class of the pure 2D and quasi-2D materials is rapidly developing [1, 2, 3, 4] regularly bringing new exciting phenomena, like observation of the 2D magnetic order [5, 6, 7], superconductivity [8, 9], and exciting optical properties [10, 11]. Among these materials, quasi-2D transition metal trichalcogenides (MPX₃, M: transition metal, X: S, Se) recently attracted increased attention because of their possible applications in many areas. It was proposed that they can be used as low-dimensional spin-polarised conductors which spin character can be tuned by the applied bias [12], in photocatalysis for the efficient water splitting and hydrogen production [13, 14, 15], as efficient materials for the Li storage [16], and, for example, the tuning of the vacancy state can lead to the low-dimensional ferromagnetic state [17].

From the crystallographic point of view, these materials are similar to, e. g., MoS₂, where one third of the metal atoms is substituted by P–P dimers and in this case the metal layer in MPX₃ is encapsulated by both chalcogens and phosphorus atoms (Fig. 1).

Diversity in transition metals and two different chalcogens can lead to a wide variation in the electronic and magnetic properties of these materials. Also, the simultaneous presence of sulphur and phosphorus in these compounds can cause a synergetic effect on the electronic structure of the central metal atoms. Moreover, due to the layered structure of MPX_3 , they can be easily prepared as two-dimensional nanostructures having a large surface area with large number of active sites. Surprisingly, the electronic structure of these materials is mainly addressed only from the theory side and the experimental studies are very rear and sporadically appear in the literature [18], moreover not always correctly interpreting the obtained experimental data [19, 20]. Also, the influence of vacancies as well as ambient adsorbates on the magnetic and electronic properties of MPX_3 are not studied at all.

Here, we present state-of-the-art density functional theory (DFT) studies of Cr-based phosphorus trichalcogenides (CrPS_3 and CrPSe_3). These materials were recently synthesised and studied with respect to their electrochemical sensing and energy applications [20]. In our work we address many aspects of these materials, like stability, chalcogen defects formation and adsorption of water molecules on pristine and defective 2D CrPX_3 layer. We found that in all cases, the electronic structure around the top of the valence band of CrPX_3 remains insensitive and main modifications are connected with the valence states redistributions at large binding energies. These results demonstrate that CrPX_3 are robust to the external factors, like chalcogen defects formation and ambient molecules adsorption, that can be utilised in future applications of these materials as, e. g., protective coatings or inert barriers for molecules.

2. Computational details

Spin-polarised DFT calculations based on plane-wave basis sets of 500 eV cutoff energy were performed with the Vienna *ab initio* simulation package (VASP). [21, 22, 23] The Perdew-Burke-Ernzerhof (PBE) exchange-correlation functional [24] was employed. The electron-ion interaction was described within the projector augmented wave (PAW) method [25] with Cr ($3p$, $3d$, $4s$), P ($3s$, $3p$), S ($3s$, $3p$) and Se ($4s$, $4p$) states treated as valence states. The Brillouin-zone integration was performed on Γ -centred symmetry reduced Monkhorst-Pack meshes using a Gaussian smearing with $\sigma = 0.05$ eV, except for the calculation of total energies. For these calculations, the tetrahedron method with Blöchl corrections [26] was employed. The $12 \times 12 \times 4$ and $24 \times 24 \times 1$ k -meshes were used for the studies of bulk and monolayer CrPX_3 , respectively, and the $12 \times 12 \times 1$ k -mesh was used for the (2×2) supercells consisting of 4-fold unit monolayers. The DFT+ U scheme [27, 28] was adopted for the treatment of Cr $3d$ orbitals, with the parameter $U_{\text{eff}} = U - J$ equal to 4 eV. Dispersion interactions were considered adding a $1/r^6$ atom-atom term as parameterised by Grimme (“D2” parameterisation) [29]. This approach yields structural parameters, which are in good agreement with available experimental data [20].

When modelling CrPX_3 monolayers, the lattice constant in the lateral plane was

set according to the optimised lattice constant of bulk CrPX₃. A vacuum gap was set to approximately 26 Å. During structure optimisation, the convergence criteria for energy and force were set equal to 10⁻⁵ eV and 10⁻² eV/Å, respectively.

The cleavage energy was calculated as

$$E_{\text{cl}} = (E_{d_0 \rightarrow \infty} - E_0) / A, \quad (1)$$

where d_0 is the van der Waals gap of bulk crystal and A is the in-plane area.

To extract the exchange interaction parameters between Cr ions spins, the Heisenberg Hamiltonian was considered

$$H = \sum_{\langle i,j \rangle} J_1 \vec{S}_i \cdot \vec{S}_j + \sum_{\langle\langle i,j \rangle\rangle} J_2 \vec{S}_i \cdot \vec{S}_j + \sum_{\langle\langle\langle i,j \rangle\rangle\rangle} J_3 \vec{S}_i \cdot \vec{S}_j, \quad (2)$$

where \vec{S}_i is the net spin magnetic moment of the Cr ions at site i , three different distance magnetic coupling parameters were estimated, considering one central Cr ions interacted with three nearest neighbouring (NN, J_1), six next-nearest neighbouring (2NN, J_2), and three third-nearest neighbouring (3NN, J_3) Cr ions, respectively. Here, the long-range magnetic exchange parameters (J) can be obtained as [30]

$$\begin{aligned} J_1 &= \frac{(E_{\text{sAFM}} - E_{\text{zAFM}}) + (E_{\text{nAFM}} - E_{\text{FM}})}{16S^2}, \\ J_2 &= \frac{(E_{\text{zAFM}} + E_{\text{sAFM}}) - (E_{\text{nAFM}} + E_{\text{FM}})}{32S^2}, \\ J_3 &= \frac{3(E_{\text{zAFM}} - E_{\text{sAFM}}) + (E_{\text{nAFM}} + E_{\text{FM}})}{48S^2}, \end{aligned} \quad (3)$$

where S is the calculated magnetic moment of the Cr ion and E_{FM} , E_{nAFM} , E_{zAFM} , E_{sAFM} are the total energies in ferromagnetic, Néel antiferromagnetic, zigzag antiferromagnetic, and stripy antiferromagnetic configurations, respectively.

To estimate T_{N} temperature, Monte Carlo simulations were performed within the Metropolis algorithm with periodic boundary conditions [31]. The three exchange parameters J_1 , J_2 and J_3 were used in a 64×64 superlattice containing a large enough amount of magnetic sites to accurately evaluate the value. Upon the heat capacity $C_v(T) = (\langle E^2 \rangle - \langle E \rangle^2) / k_B T^2$ reaching the equilibrium state at a given temperature, the T_{N} value can be extracted from the peak of the specific heat profile.

The electrically neutral vacancies were created by removing one or two X atoms from the (2×2) supercells. Thereby, the distance between repeated vacancies in the nearest-neighbour cells is larger than 10 Å. The defect formation energy is defined as follows

$$\Delta E_{\text{def}} = \frac{1}{n} [E(\text{CrPX}_{3-n}) + n \mu_{\text{X}} - E(\text{CrPX}_3)], \quad (4)$$

where n is a number of defects, $E(\text{CrPX}_{3-n})$ and $E(\text{CrPX}_3)$ are the energies of the 2D CrPX₃ with and without vacancy, respectively, μ_{X} is the chemical potential of X atom ($\mu_{\text{S}} = -4.1279$ eV and $\mu_{\text{Se}} = -3.4895$ eV).

To study the adsorption of a single molecule, a (2×2) supercell was used with one water molecule added. Adsorption energies were calculated as

$$\Delta E_{\text{ads}} = E(\text{A/CrPX}_3) - [E(\text{A}) + E(\text{CrPX}_3)], \quad (5)$$

where $E(\text{CrPX}_3)$ and $E(\text{A})$ are the energies of the isolated 2D CrPX_3 and an adsorbate, and $E(\text{A}/\text{CrPX}_3)$ is the energy of their interacting assembly.

3. Results and Discussion

3.1. 3D CrPX_3 ($X = \text{S}, \text{Se}$)

3D bulk MPX_3 crystals usually adopt either an *AAA* stacking in $C2/m$ space group space or *ABC* stacking in $R\bar{3}$ space group. Both of them can be represented in hexagonal unit cells (Fig. 1 a). Then every unit cell contains three MPX_3 single layers which have D_{3d} symmetry (see Fig. 1 b,c), which are stacked in a different way. Each single-layer are held together by van der Waals forces. The lattice parameters of hexagonal 3D CrPX_3 were fully relaxed in nonmagnetic (NM), ferromagnetic (FM) and Néel antiferromagnetic (nAFM) states and they are listed in Table 1 with the respective total energies. Thus, both CrPX_3 ($X = \text{S}, \text{Se}$) prefer the $C2/m$ symmetry, that is in agreement with available experimental data [32]. For both CrPS_3 and CrPSe_3 , the energetically most favourable structure corresponds to the nAFM configuration (Tab. 1). The band structure and density of states (DOS) calculated for the ground-state structures of 3D CrPS_3 and CrPSe_3 are shown in Figure 2 (a) and (b), respectively. From these results one can see, that the both systems under study are indirect band gaps semiconductors. The band gaps obtained by the PBE+ U method are 1.11 eV for bulk CrPS_3 and 0.70 eV for bulk CrPSe_3 . The upper valence bands (VBs) are mainly formed by S/Se p and equal to that by the Cr $3d$ orbitals; the lower conduction bands (CBs) are composed of Cr $3d$ states with somewhat contribution from S/Se p . The partial contributions from P p orbitals are very small in VBs as well as CBs. These results are very different from the respective data known for MnPX_3 [33] and NiPX_3 [18, 34], where the contribution of metal $3d$ states in VBs was insignificant.

It is expected that individual CrPX_3 layers can be isolated by mechanical exfoliation. In this regard, the cleavage energy (E_{cl}) of a layered material is an essential property that need to be considered. The calculated values, $E_{\text{cl}}(\text{CrPS}_3) = 0.18 \text{ J m}^{-2}$ and $E_{\text{cl}}(\text{CrPSe}_3) = 0.23 \text{ J m}^{-2}$ (Fig. 3, left panel), are smaller than that of a bulk graphite (0.36 J m^{-2}) [35], which is used as an indicator for the feasibility of exfoliation of materials in experiments. The obtained values are in the same range as recently published for MnPX_3 and NiPX_3 [33, 34].

3.2. 2D CrPX_3 ($X = \text{S}, \text{Se}$) monolayers

Four possible magnetic configurations were investigated to evaluate the ground state of 2D CrPX_3 monolayers: The mentioned above FM (Fig. 4 a), and nAFM (Fig. 4 b) were supplemented by a zig-zag AFM (zAFM, Fig. 4 c) and a stripy AFM (sAFM, Fig. 4 d). The obtained results are listed in Table 2. It can be seen that the lowest energy configurations for the 2D CrPX_3 ($X = \text{S}, \text{Se}$) monolayers are the Néel AFM states.

The 2D CrPS₃ and CrPSe₃ in their ground states keep an indirect semiconductor behaviour (Fig. 2c,d). Due to the quantum confinement effects, the band gaps are slightly larger than the values calculated for the bulk phases and are 1.52 eV and 1.11 eV for the 2D CrPS₃ and CrPSe₃, respectively. As for the bulk materials, the bands in the vicinity of Fermi energy are mostly composed of Cr-*d* and S/Se-*p* orbitals.

The exchange-coupling parameters (J_1, J_2, J_3) describing the magnetic interactions between Cr²⁺ ions were calculated according to eqn. (3) and are listed in Tab. 2. According to the Goodenough-Kanamori-Anderson (GKA) rules [36, 37], the origin of the nAFM ground state can be attributed to the competition between the NN AFM direct Cr–Cr (*d* – *d*) exchange interactions and the indirect Cr–Se···Se–Cr (*p* – *d*) superexchange interactions [38]. The calculated J parameters were used in the Monte-Carlo simulations of Néel temperatures of CrPX₃ monolayers. The estimated T_N is 190 K for 2D CrPS₃ and 119 K for 2D CrPSe₃ (Fig. 3, right panel). These results are in very good agreement with the experimental result available for CrPSe₃, that is: $T_N = 136$ K [20].

3.3. Chalcogen defects

Mechanical exfoliation used for monolayers production, can lead to formation of chalcogen vacancies. Therefore, we consider three different kinds of defects: (i) one vacancy at X-site, named as V_X@1L with a defect concentration about 2.5 % (Fig. 1 c); (ii) two vacancies at the neighbouring X-sites of the same chalcogen sublayer named as V_{X2}@1L with a concentration about 5 % (Fig. 1 d); (iii) two vacancies at X-sites of the different chalcogen sub-layers named as V_{X2}@2L with a concentration about 5 % (Fig. 1 e). The defect formation energies (Tab. 3) are of the same order that is known for the other MPX₃ family members [33, 34] and are rather low in all cases presumably indicating a feasibility of formation of these kinds of defects in experiments. According to the defect formation energies, it is found that V_X@1L defects are the most favourable to form, followed by V_{2X}@2L and V_{2X}@1L. Also, we can observed that for the same defect type, Se vacancy is more likely to occur than S vacancy, which correlates with the respective electronegativity values. Although the rather low ΔE_{def} obtained for all considered cases, we expect that in experimental conditions the formation of single chalcogen defects is more feasible and from now on we will focus on detailed consideration of V_X@1L.

Removal of chalcogen atom leads to some modifications of the local lattice and electronic structures. As compared to the pristine CrPX₃ monolayer, the phosphorous dimers tend to moving closer to the vacancy. The angle, which P–P dimer forms with the vertical direction is 2.5° and 3.9° for X = S and Se, respectively. The dimer is pulled out from a monolayer. This leads to somewhat increase of the P–S bond length (by ≈ 0.05 Å), while the P–P bond lengths remain basically unchanged.

The electrons left behind upon removal of a chalcogen atom, occupy the easily available electronic states of a (P₂X₅) entity. The magnetic moments of the Cr²⁺-ions

nearby the vacancy are coupled antiferromagnetically. Similarly to the data recently published for MnPX_3 [33], there are no well-localised defect state generated within the band gap in the DOS (Fig. 5). As a result, the energy gap width of the defective monolayers stays almost unchanged regarding the pristine CrPX_3 : $E_g = 1.41$ eV and 1.02 eV for the defective CrPS_3 and CrPSe_3 , respectively. At the same time, at $E - E_F \approx -0.55$ eV a new state appears, which is formed by S/Se p and equal to that by the Cr $3d$ orbitals.

The estimated T_N value for the defective trichalcogenide monolayers is reduced to 158 K and 69 K for CrPS_3 and CrPSe_3 , respectively (Fig. 3). This effect is generally expected because the X-vacancy formation leads to the drastic reduction of the J exchange-coupling parameters ($J_1 = -2.76$ meV, $J_2 = 0.03$ meV, $J_3 = 0.20$ meV for CrPS_{3-x} ; $J_1 = -1.59$ meV, $J_2 = 0.02$ meV, $J_3 = 0.28$ meV for CrPSe_{3-x}). At the same time the strongly localised magnetic moments of Cr^{2+} ions remain the same.

3.4. Adsorption of H_2O

The effect of adsorption of molecular water plays an important role in various applications and technological processes, since they are present in the environment of any device. Thus in the next step we investigate how adsorption of H_2O affects the electronic properties of CrPX_3 monolayers.

Various high-symmetry adsorption sites and adsorption orientations are taken into account. Considering the pristine monolayers, all adsorption configurations have similar adsorption energies which range from -133 meV to -153 meV and from -148 meV to -166 meV for 2D CrPS_3 and 2D CrPSe_3 , respectively. In the relaxed structures water stays almost parallel to the substrate and the vertical distance between the molecule and the CrPX_3 monolayer is always above 3.2 \AA .

For pristine monolayers, in the most stable adsorption structure (**AS1**, Fig. 6a), a water molecule attaches with its oxygen atom to an P atom [$d(\text{P-O}) = 3.23 \text{ \AA}$ and 3.32 \AA for CrPS_3 and CrPSe_3 , respectively] and the H atoms are directed towards the neighbouring X atoms. In accordance with the weak interaction, the structural parameters of H_2O as well as of the studied monolayer undergo insignificant changes. As follows from the electron density redistribution plot (Fig. 6a), upon adsorption the main charge rearrangement takes place between O and P atoms. Charge accumulation in the p -orbital of P on the side of the adsorbate indicates that it is the main orbital participating in the bonding. This charge accumulation is accompanied with a depletion at the hydrogen positions. These observation are in line with the effects arising in DOS due to the interaction between H_2O and CrPX_3 (Fig. 6e): Hybridisation between p states of P and the water lone pair [$3a_1$ molecular orbital (MO) of H_2O] takes place, that results in broadening of the respective water derived states. Besides, a slight upward shift with respect to the MO of gas phase water molecule is observed. The obtained results on the adsorption of H_2O on pristine CrPX_3 are in general trend observed for graphene and for the other 2D chalcogenides. The adsorption energies for H_2O on graphene, MoS_2 , and

WS₂ are $-0.12\dots -0.14$ eV, -0.15 eV, and -0.15 eV, respectively [39, 40, 41], indicating the physisorption nature of interaction.

Considering the defective monolayers, the situation is more interesting. Firstly, the adsorption structure similar to **AS1** exists. It is abbreviated as **AS2** and presented in Figure 6b. In this case, the interaction between H₂O and the substrate is stronger ($E_{\text{ads}} = -219$ meV and $E_{\text{ads}} = -224$ meV), which is reflected by the reduced distance $d(\text{P-O}) = 2.85$ Å and 2.98 Å for CrPS₃ and CrPSe₃, respectively. In the rest, the electronic structures of the molecule and substrate undergo qualitatively similar changes as in the case of **AS1** (Fig. 6f).

In addition to **AS2**, a structure, called **AS3** was investigated, where water molecule is coordinated between two Cr ions as it is shown in Figure 6c. (Similar configuration was found to be the energetically most favourable when studying water adsorption on NiPX_{3-x} [34]). Charge accumulation is observed between O and two Cr atoms as well as between H and P atom, which lost the chalcogen neighbour (Fig. 6c). Significant contribution of the the $1b_1$ and $3a_1$ MOs to the bonding with the monolayer is expressed in their substantial broadening due to hybridisation with P-*p* sates. The healing of vacancy is accompanied by shift of the the defect derived state from its original position to lower binding energies where it is mixed with the valence band states.

The interaction between between H and P atoms in **AS3** has one important effects on the geometric structure: A significant elongation of the H–O bond from 0.97 Å for the gas-phase molecule to 1.06 Å and 1.04 Å for the adsorbed molecule on CrPS_{3-x} and CrPSe_{3-x}, respectively. A further H–O bond elongation up to $d(\text{O-H}) = 2.02$ Å leads to structure **AS4** (Fig. 6d), which is slightly higher in energy as compared to **AS3**. Here the P–H bond is formed ($d(\text{P-H}) = 1.40$ Å). Similarly to recently published results for NiPX₃ [34], the corresponding structure was found to be unstable for CrPSe_{3-x}. The weaker adsorbate-substrate interaction in the case of **AS4** is reflected by less pronounced changes in the DOS of the interacting species. By that the qualitative tendency of the induced modifications in **AS4** is similar to **AS3**.

4. Conclusions

In conclusions, we performed systematic DFT studies of pristine and chalcogen-defective 2D CrPX₃ (X: S, Se). It is shown that both pristine materials are wide gap semiconductors in the ground state with a band gap of 1.52 eV and 1.11 eV, respectively. The chalcogen vacancies are characterised by very strongly localised defect states located at ≈ 0.5 eV below the valence band maximum and in the gap formed by valence band states, indicating the minimal influence of such defects on the optical and transport properties of CrPX₃. The adsorption of H₂O on the pristine and chalcogen-defective 2D CrPX₃ layers is always described as a physisorption, with possible water splitting. However, the clear preferential adsorption of H₂O on all kinds of surfaces of CrPX₃, molecular or dissociative, is not observed. It is found that in all cases of the surface modifications (chalcogen vacancies or ambient molecules adsorption),

the electronic structure of CrPX₃ remains robust against these factors, indicating the possible application of these materials as effective protecting coatings.

- [1] Zeng M, Xiao Y, Liu J, Yang K and Fu L 2018 *Chem Rev* **118** 6236–6296
- [2] Akinwande D, Huyghebaert C, Wang C H, Serna M I, Goossens S, Li L J, Wong H S P and Koppens F H L 2019 *Nature* **573** 507–518
- [3] Dedkov Y S and Voloshina E 2020 *Nanoscale* **12** 11416–11426
- [4] Andrei E Y and MacDonald A H 2020 *Nat. Mater.* 1265–1275
- [5] Lee J U, Lee S, Ryoo J H, Kang S, Kim T Y, Kim P, Park C H, Park J G and Cheong H 2016 *Nano Lett.* **16** 7433–7438
- [6] Wang X, Du K, Liu Y Y F, Hu P, Zhang J, Zhang Q, Owen M H S, Lu X, Gan C K, Sengupta P, Kloc C and Xiong Q 2016 *2D Mater.* **3** 031009
- [7] Gong C, Li L, Li Z, Ji H, Stern A, Xia Y, Cao T, Bao W, Wang C, Wang Y, Qiu Z Q, Cava R J, Louie S G, Xia J and Zhang X 2017 *Nature* **546** 265–269
- [8] Cao Y, Fatemi V, Fang S, Watanabe K, Taniguchi T, Kaxiras E and Jarillo-Herrero P 2018 *Nature* **556** 43–50
- [9] Cao Y, Fatemi V, Demir A, Fang S, Tomarken S L, Luo J Y, Sanchez-Yamagishi J D, Watanabe K, Taniguchi T, Kaxiras E, Ashoori R C and Jarillo-Herrero P 2018 *Nature* **556** 80–84
- [10] Kang S, Kim K, Kim B H, Kim J, Sim K I, Lee J U, Lee S, Park K, Yun S, Kim T, Nag A, Walters A, Garcia-Fernandez M, Li J, Chapon L, Zhou K J, Son Y W, Kim J H, Cheong H and Park J G 2020 *Nature* **583** 785–789
- [11] Ma Q, Ren G, Xu K and Ou J Z 2021 *Adv. Opt. Mater* **9** 2001313
- [12] Li X, Wu X and Yang J 2014 *J. Am. Chem. Soc.* **136** 11065–11069
- [13] Cheng Z, Shifa T A, Wang F, Gao Y, He P, Zhang K, Jiang C, Liu Q and He J 2018 *Adv. Mater.* **30** 1707433
- [14] Cheng Z, Sendeku M G and Liu Q 2020 *Nanotechnology* **31** 135405
- [15] Du C F, Liang Q, Dangol R, Zhao J, Ren H, Madhavi S and Yan Q 2018 *Nano-Micro Lett.* **10** 67
- [16] Fan C Y, Zhang X H, Shi Y H, Xu H Y, Zhang J P and Wu X L 2019 *J. Mater. Chem. A* **7** 1529–1538
- [17] Bai W, Hu Z, Xiao C, Guo J, Li Z, Zou Y, Liu X, Zhao J, Tong W, Yan W, Qu Z, Ye B and Xie Y 2020 *J. Am. Chem. Soc.* **142** 10849–10855
- [18] Yan M, Jin Y, Wu Z, Tsaturyan A, Makarova A, Smirnov D, Voloshina E and Dedkov Y 2021 *J. Phys. Chem. Lett.* **12** 2400–2405
- [19] Dedkov Y S, Yan M and Voloshina E 2020 *Chem. Phys. Lett.* **754** 137627
- [20] Gusmão R, Sofer Z, Sedmidubský D, Huber Š and Pumera M 2017 *ACS Catal.* **7** 8159–8170
- [21] Kresse G and Furthmüller J 1996 *Comp. Mater. Sci.* **6** 15–50
- [22] Kresse G and Hafner J 1994 *J. Phys.: Condens. Matter* **6** 8245–8257
- [23] Kresse G and Hafner J 1993 *Phys. Rev. B* **47** 558–561
- [24] Perdew J P, Burke K and Ernzerhof M 1996 *Phys. Rev. Lett.* **77** 3865–3868
- [25] Blöchl P E 1994 *Phys. Rev. B* **50** 17953–17979
- [26] Blöchl P E, Jepsen O and Andersen O K 1994 *Phys. Rev. B* **49** 16223–16233
- [27] Anisimov V I, Aryasetiawan F and Lichtenstein A I 1997 *J. Phys.: Condens. Matter* **9** 767–808
- [28] Dudarev S L, Botton G A, Savrasov S Y, Humphreys C J and Sutton A P 1998 *Phys. Rev. B* **57** 1505–1509
- [29] Grimme S 2006 *J. Comput. Chem.* **27** 1787–1799
- [30] Sivadas N, Daniels M W, Swendsen R H, Okamoto S and Xiao D 2015 *Phys. Rev. B* **91** 235425
- [31] Metropolis N, Rosenbluth A W, Rosenbluth M N, Teller A H and Teller E 1953 *J. Chem. Phys.* **21** 1087–1092
- [32] Brec R, Ouyard G, Louisy A and Rouxel J 1980 *Ann. Chim.* **5** 499–512
- [33] Yang J, Zhou Y, Guo Q, Dedkov Y S and Voloshina E 2020 *RSC Adv.* **10** 851–864
- [34] Wu Z, Xu S, Zhou Y, Guo Q, Dedkov Y and Voloshina E (submitted)

- [35] Zacharia R, Ulbricht H and Hertel T 2004 *Phys. Rev. B* **69** 155406
- [36] Goodenough J B 1955 *Phys. Rev. B* **100** 564–573
- [37] Kanamori J 1960 *J. Appl. Phys.* **31** S14–S23
- [38] Yang J, Zhou Y, Dedkov Y S and Voloshina E 2020 *Adv. Theory Simul.* **3** 2000228
- [39] Voloshina E, Usvyat D, Schütz M, Dedkov Y and Paulus B 2011 *Phys. Chem. Chem. Phys.* **13** 12041–12047
- [40] Levita G, Restuccia P and Righi M C 2016 *Carbon* **107** 878–884
- [41] Bui V Q, Pham T-T, Le D A, Thi C M and Le H M 2015 *J. Phys.: Condens. Matter* **27** 305005

Table 1. Results obtained for the different magnetic states of 3D CrPS₃ and CrPSe₃ with PBE+*U*+D2: *E* (in eV) is the total energy per unit cell, *a, c* (in Å) are the optimised lattice parameters, *d*₀ (in Å) is the van der Waals gap of bulk crystal.

X	Symmetry	Magnetic state	<i>E</i>	<i>a</i>	<i>c</i>	<i>d</i> ₀
S	<i>C</i> 2/ <i>m</i>	NM	−150.706	5.75	19.35	3.32
		FM	−167.336	6.01	19.48	3.27
		nAFM	−168.501	6.01	19.48	3.21
	<i>R</i> $\bar{3}$	NM	−150.083	5.75	19.35	3.33
		FM	−167.300	6.01	19.48	3.26
		nAFM	−166.507	6.01	19.48	3.21
Se	<i>C</i> 2/ <i>m</i>	NM	−134.846	6.16	19.44	3.30
		FM	−153.804	6.35	19.94	3.26
		nAFM	−154.568	6.35	19.94	3.20
	<i>R</i> $\bar{3}$	NM	−134.901	6.16	19.44	3.32
		FM	−153.137	6.35	19.94	3.25
		nAFM	−153.141	6.35	19.94	3.20

Table 2. Results obtained for the different magnetic states of 2D CrPS₃ and CrPSe₃ with PBE+*U*+D2: E_{tot} (in eV per (2×2) unit cell) is the total energy; ΔE (in meV) is the difference between the total energy calculated for the magnetic states and the total energy calculated for the nAFM state. Band gap (E_g , in meV), Cr²⁺ magnetic moment (M , in μ_B), the exchange coupling parameters between two local spins (J , in meV), and Néel temperature (T_N , in K) are given for the lowest-energy structure.

X	Magn. state	E_{tot}	ΔE	E_g	M	J_1	J_2	J_3	T_N
S	FM	-223.260	480						
	nAFM	-223.740	0	1.52	3.8	-3.10	0.14	0.32	190
	sAFM	-223.587	153						
	zAFM	-223.351	389						
Se	FM	-204.172	294						
	nAFM	-204.466	0	1.11	3.8	-2.06	0.15	0.36	119
	sAFM	-204.375	91						
	zAFM	-204.194	272						

Table 3. Defect formation energies (ΔE_{def} , in eV) obtained for the CrPX_{3-x} monolayers.

Defect type	X = S	X = Se
$V_X@1L$	1.069	0.810
$V_{X_2}@1L$	1.222	1.120
$V_{X_2}@2L$	1.098	0.863

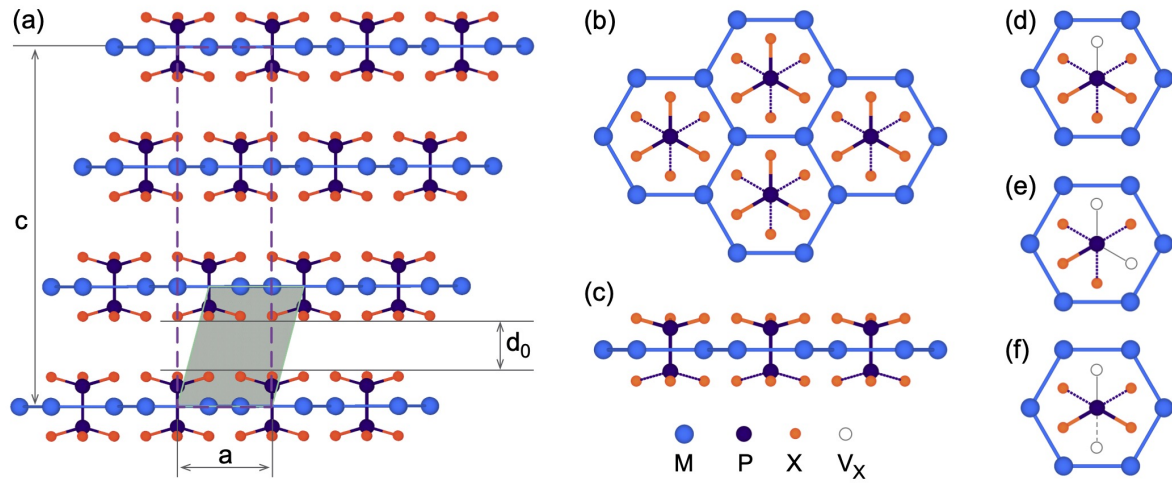


Figure 1. (Left panel) (a) Crystal structure of 3D MPX_3 . Dashed line denotes the hexagonal unit cell used in the present work. The in-plane and out-of-plane lattice constants are indicated with letters a and c , respectively. Shaded area denotes a primitive unit cell. Distance d_0 corresponds to the van-der-Waals gap. Spheres of different size/colour represent ions of different type. (Middle panel) Top (b) and side (c) views of a single layer of MPX_3 . (Right panel) The considered chalcogen defects: (d) $V_X@1L$; (e) $V_{X_2}@1L$; (f) $V_{X_2}@2L$.

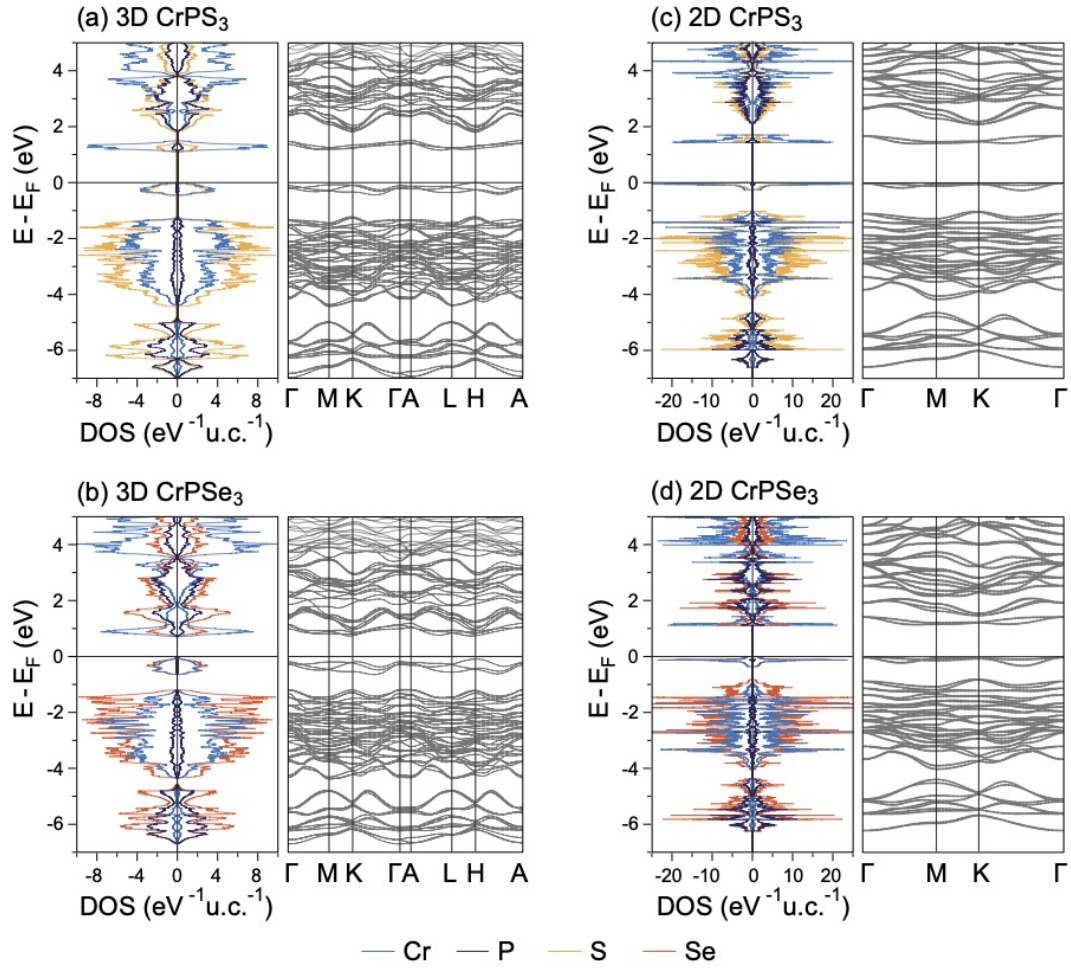


Figure 2. Band structure and site-projected density of states for (a) 3D CrPS₃ bulk, (b) 3D CrPSe₃ bulk, (c) 2D CrPS₃ monolayer, and (d) 2D CrPSe₃ monolayer.

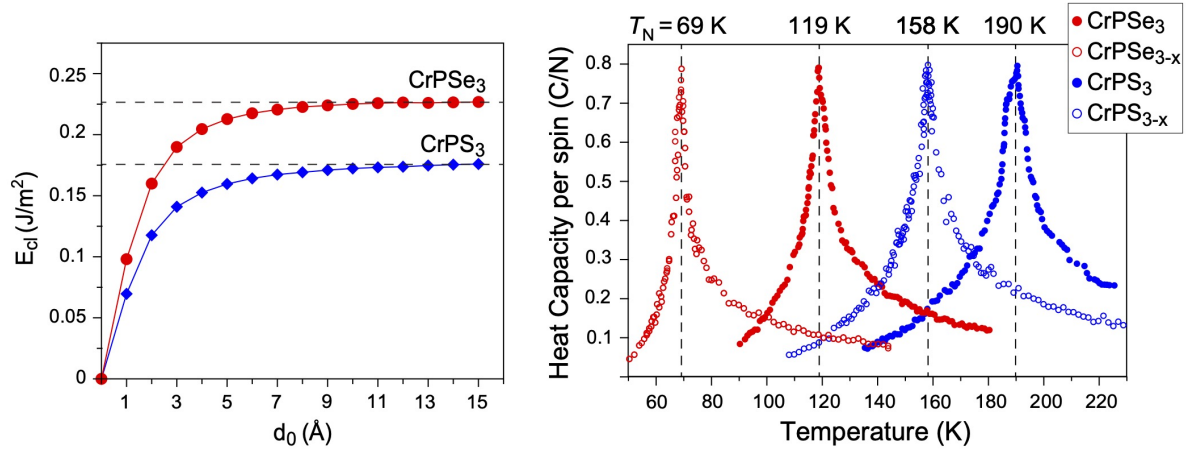


Figure 3. (Left panel) Cleavage energy of 3D CrPX_3 (E_{cl}) as a function of the van der Waals gap (d_0). (Right panel) Specific heat capacity per spin with respect to temperature for 2D CrPX_3 and CrPX_{3-x} .

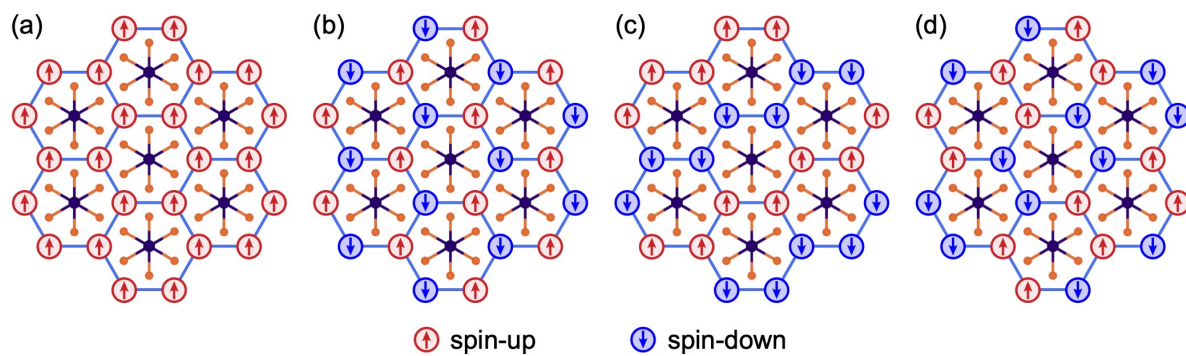


Figure 4. Four different magnetic configurations of 2D CrPX₃: (a) ferromagnetic (FM), (b) Néel antiferromagnetic (nAFM), (c) zigzag antiferromagnetic (zAFM), and (d) stripy antiferromagnetic (sAFM).

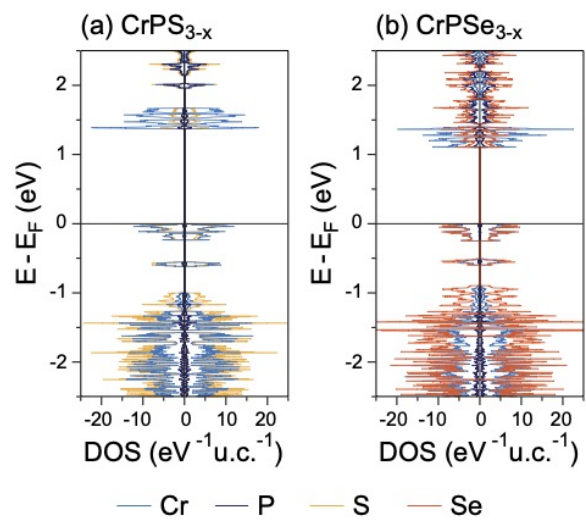


Figure 5. Site-projected density of states for the defective monolayers: (a) 2D CrPS_{3-x} and (b) 2D CrPSe_{3-x} .

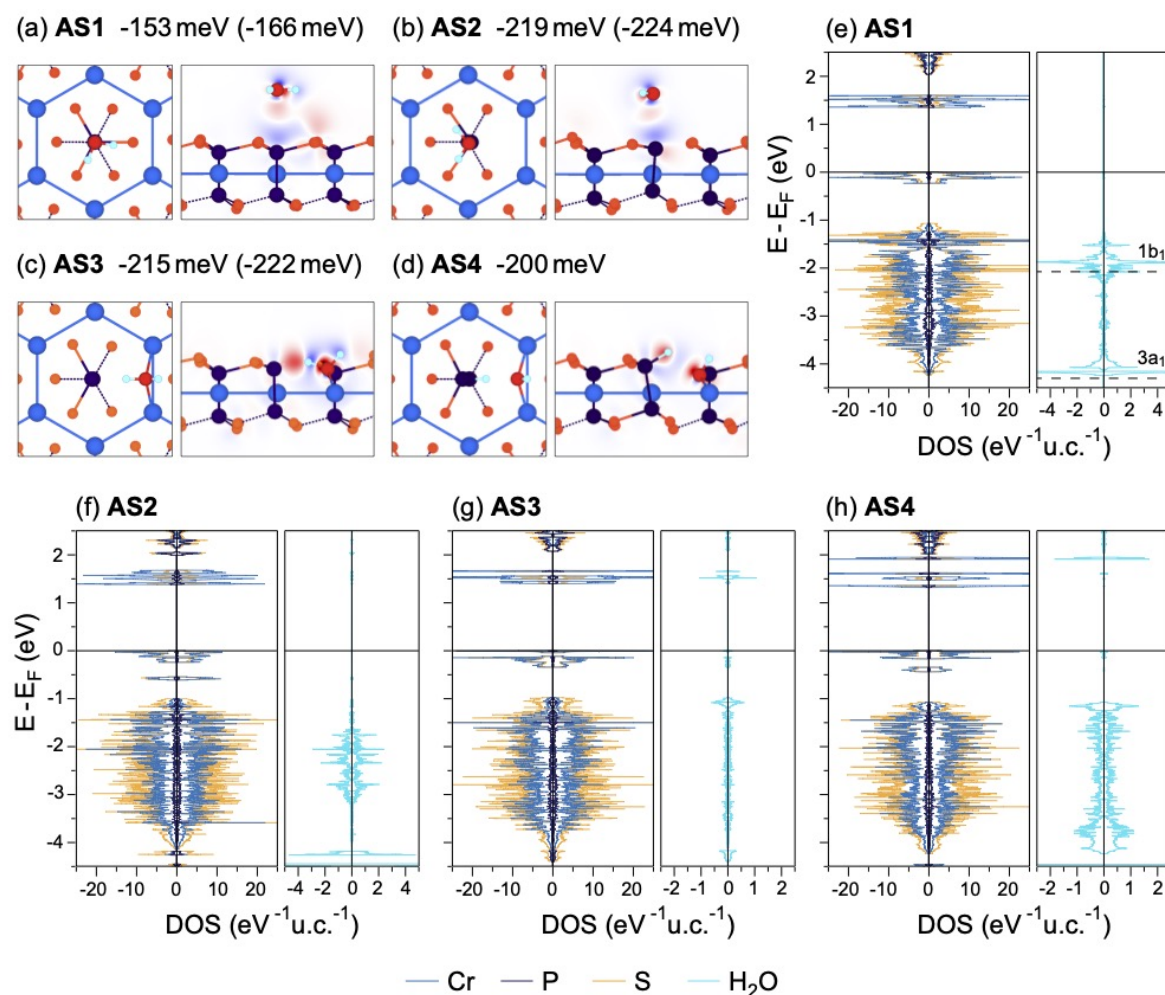


Figure 6. (a-d) Top and side views of the relaxed structures obtained after water adsorption on pristine and defective CrPX₃ (cf. text for details). Side view are superimposed with electron density redistribution maps. Electron density accumulation (depletion) is shown in red (blue). Blue, violet, and orange spheres represent Cr, P, and X atoms, respectively. The water molecule is shown with red and light-blue spheres, for O and H, respectively. The adsorption energies are given above each adsorption structure for X=S (X=Se). (e-h) Site-projected density of states obtained for the structures presented in (a-d) where X = S. In (e), the molecular orbitals of a gas-phase H₂O molecule are indicated by horizontal dashed lines. These are obtained by aligning the $2a_1$ core level of the gas-phase and adsorbed H₂O molecules.